Superconducting-qubit gates robust to parameter fluctuations

E.M. Wright,[1,2,3,*] L. Van Damme,[1,4] N.J. Glaser,[1,2] A. Devra,[1,4] F.A. Roy,[2,5] J. Englhardt,[1,2] N. Bruckmoser,[1,2] L. Koch,[1,2] A. Marx,[1,2] J. Schirk,[1,2] C.M.F. Schneider,[1,2] L. Södergren,[1,2] I. Tsitsilin,[1,2] F. Wallner,[1,2] S.J. Glaser,[1,4] M. Werninghaus,[1,2,†] and S. Filipp[1,2,4]

[1] *Technical University of Munich, Garching, Germany*
[2] *Walther-Meißner-Institut, Garching, Germany*
[3] *International Max Planck Research School for Quantum Science and Technology, Garching, Germany*
[4] *Munich Center for Quantum Science and Technology, Munich, Germany*
[5] *Saarland University, Saarbrücken, Germany*

(Received 9 January 2026; revised 12 March 2026; accepted 2 April 2026; published 14 May 2026)

State-of-the-art single-qubit gates on superconducting transmon qubits can achieve the fidelities required for error-corrected computations; however, parameter fluctuations due to qubit instabilities, environmental changes, and control inaccuracies make it difficult to maintain this performance. To mitigate the effects of these parameter variations, we numerically derive gates that are robust to amplitude and frequency errors using gradient-ascent pulse engineering. We analyze how fluctuations in qubit frequency, drive amplitude, and coherence affect gate performance over time. The robust pulses suppress coherent errors from drive-amplitude drifts over 15 times more than a Gaussian pulse with derivative removal by adiabatic gate (DRAG) corrections. Furthermore, the robust gates, originally designed to compensate for quasistatic errors, also demonstrate resilience to stochastic, time-dependent noise, which is reflected in the dephasing time. They suppress added errors during increases in dephasing by up to 1.7 times more than DRAG.

DOI: 10.1103/tf39-n6s3

I. INTRODUCTION

Superconducting qubits have emerged as a leading platform for scalable, error-corrected quantum processors that operate at high speed [1–3]. In particular, they support fast single-qubit gate operations that can meet the fidelity threshold for scalable quantum error correction (QEC) [3,4]; however, maintaining the required level of performance is challenging due to instabilities arising from environmental disturbances and drifts in control hardware that lead to both coherent and stochastic errors [5].

Coherent errors can arise from persistent parameter offsets, such as crosstalk [6] and miscalibrations. They can also occur due to quasistatic drifts that are effectively constant over the duration of an experiment, for example, slow fluctuations in the qubit frequency [7] and instabilities in control electronics [8]. These errors are difficult to detect or correct with conventional QEC codes, which are designed primarily to address random Pauli noise [5,9,10]. In contrast to coherent errors, stochastic errors fluctuate randomly in time, leading to decoherence. They originate from sources such as two-level systems (TLSs) [11,12], ionizing radiation [13], and quasiparticles [14], and they can cause fluctuations in qubit coherence times and frequency [7,15]. Changes in the energy relaxation time T_1, often linked to interactions with TLSs, occur unpredictably on millisecond-to-hour timescales [16,17] and exhibit spatiotemporal correlations associated with radiation events [18–20]. Similar behavior is observed for the dephasing time T_ϕ, where rapid frequency fluctuations from dispersive interactions with TLSs and from quasiparticle tunneling lead to significant reductions in coherence [7,21]. These stochastic errors degrade quantum processor performance and reduce the effectiveness of QEC, often necessitating postselection to discard data affected by low coherence [4,22,23]. Robust gate designs that inherently

*Contact author: emily.wright@wmi.badw.de
†Contact author: max.werninghaus@wmi.badw.de

Published by the American Physical Society under the terms of the Creative Commons Attribution 4.0 International license. Further distribution of this work must maintain attribution to the author(s) and the published article's title, journal citation, and DOI.

tolerate parameter fluctuations offer a promising path to mitigating both coherent and stochastic errors.

Several methods have been demonstrated for realizing robust gates, including open-loop optimization [24–29], geometric gates [30–34], composite pulses [35–38], sampling-based learning control [39–41], and other advanced optimization methods [42–47]. Robust gates can be designed to combat fluctuations in various parameters, including drive amplitude [25–29,31–37,41–43], qubit frequency [25–29,32–37,42–44], and qubit-qubit coupling [28–30,37,39,40]. While robust gates consistently reduce coherent errors in experiments [25,26,31–33,41–43], their behavior in complex noise environments remains less understood [47]. Previous simulations have shown that robust gates, even those designed only for static errors, can offer resilience against stochastic, time-varying noise [24,28,38]. Indeed, robust gates have been shown to help stabilize operation fidelity over time [26]; however, experimentally demonstrating and quantifying their robustness under realistic operating conditions remains a challenge.

In this work, we design two robust gates for superconducting transmon qubits through gradient-ascent pulse engineering (GRAPE) [48,49]: a frequency-robust gate (FROG) and an amplitude-and-frequency-robust gate (AROG). Their robustness landscapes, measured experimentally by adding amplitude and detuning errors to the system, reveal protection in the targeted parameters compared to a standard Gaussian pulse with derivative removal by adiabatic gate (DRAG) corrections [50–52]. We further investigate operational noise—encompassing both coherent and stochastic errors—discuss potential noise sources, and analyze the individual contributions of these noise sources to gate error.

II. ROBUST GATES

A. Device and model

Experiments are carried out on a transmon-type fixed-frequency superconducting qubit [53] which has a transition frequency of $\omega_{01}/(2\pi) = 3.9872(2)$ GHz, an anharmonicity $\alpha/(2\pi) = -295.1(2)$ MHz, and a maximum Rabi rate $\Omega_0/(2\pi) = 17.7(5)$ MHz. The average coherence times are $T_1 = 45.5(1)$ μs and $T_2^* = 16.81(6)$ μs. The qubit is capacitively coupled to a readout resonator at $\omega_r/(2\pi) = 6.89041(3)$ GHz with a coupling strength of $g/(2\pi) = 72(5)$ MHz. Throughout this work, the uncertainty of fitted parameters is the expected one-standard-deviation uncertainty, derived from the diagonal elements of the covariance matrix. When time-series data are available, we report the mean of the measured values, with the uncertainty given by the standard error of the mean. Further details of the setup are provided in Appendix A.

The dynamics are described by the Hamiltonian

$$\frac{\hat{H}^{\mathrm{R}}}{\hbar} = \alpha\,|2\rangle\langle 2| + \delta\sum_{k=1}^{2} k\,|k\rangle\langle k| + \left(1+\frac{\gamma}{\Omega_0}\right) \times\left(\frac{\Omega_x(t)}{2}\sum_{k=1}^{2}\hat{\sigma}^x_{k,k-1} + \frac{\Omega_y(t)}{2}\sum_{k=1}^{2}\hat{\sigma}^y_{k,k-1}\right) \quad (1)$$

in a frame rotating at the qubit frequency ω_{01}. In simulations, we include three energy levels k with eigenstates $|k\rangle$ to capture leakage. We describe transitions between adjacent energy levels with the operators $\hat{\sigma}^x_{k,k-1} = \sqrt{k}\,(|k\rangle\langle k-1| + |k-1\rangle\langle k|)$ and $\hat{\sigma}^y_{k,k-1} = i\sqrt{k}\,(|k\rangle\langle k-1| - |k-1\rangle\langle k|)$. Pulses consist of two control components $\Omega_x(t)$ and $\Omega_y(t)$, which are combined into a single drive signal $\Omega(t) = \Omega_x(t) + i\Omega_y(t)$. To reflect fluctuations in the system parameters, we have introduced δ as a frequency error and γ as a drive-amplitude error in the Hamiltonian.

B. Numerical optimization

To compensate for frequency and amplitude errors, we derive robust gates using numerical optimization. To force the pulse to start and end at zero, ensure symmetries, and keep pulse variations slow, we choose a pulse ansatz in the Fourier basis of the form

$$\Omega_x(t) = \Omega_0\sum_{n=1}^{5} a_n \sin((2n-1)\pi t/t_g),$$
$$\Omega_y(t) = \Omega_0\sum_{n=1}^{5} b_n \sin(2n\pi t/t_g), \quad (2)$$

where a_n and b_n represent Fourier-series coefficients, t_g is the gate length, and n enumerates the Fourier components. In all cases, we optimize ten coefficients—five each for a_n and b_n—to shape the pulse defined in Eq. (2). This choice promotes smooth pulse profiles, avoiding abrupt changes or high-frequency components, which are expected to be less sensitive to pulse distortions and other undesirable effects [54].

We optimize the Fourier-series coefficients in Eq. (2) using the GRAPE algorithm adapted to analytically shaped functions [55]. GRAPE works by discretizing the time evolution under the parametrized pulse shape. The fidelity of the resulting operation is evaluated by a cost function, and gradients of this cost function with respect to the pulse parameters are computed efficiently using forward and backward propagation. The parameters are then updated iteratively along the gradient direction to increase fidelity.

To achieve robustness, we optimize over a discrete set of Hamiltonians, as defined in Eq. (1), which differ by variations in the detuning δ and amplitude γ scaling parameters.

Specifically, we consider deviations in $\delta \in [\delta_{\min}, \delta_{\max}]$ and $\gamma \in [\gamma_{\min}, \gamma_{\max}]$, sampling a finite set of values across these intervals. For each sampled pair (δ_i, γ_j), we define a corresponding perturbed Hamiltonian $H_{ij}(t)$ and simulate the system evolution. For each pair of parameters (δ_i, γ_j), we define the gate error as

$$\mathcal{E}_g^{ij} = 1 - F_g^{ij} = 1 - \frac{1}{4}\left|\sum_{k=0}^{1} \langle k| U_{\mathrm{T}}^{\dagger} U_{ij}(t_g) |k\rangle\right|^2, \quad (3)$$

where $U_{ij}(t_g)$ is the time-evolution operator at time t_g solving $\dot{U}_{ij}(t) = -H_{ij}(t)U_{ij}(t)$ and U_{T} is the target unitary. As a cost function we use the gate error averaged over the entire parameter set:

$$J = \frac{1}{N_\delta N_\gamma} \sum_{i=1}^{N_\delta} \sum_{j=1}^{N_\gamma} \mathcal{E}_g^{ij}, \quad (4)$$

where N_δ and N_γ are the number of sampled values of δ and γ, respectively. This ensemble-averaged cost ensures that the optimized pulse performs well not just for the nominal Hamiltonian but also across the expected range of deviations. By iteratively updating the pulse shape using the gradient of the average cost with respect to the control parameters, the GRAPE algorithm converges to a solution that is robust to fluctuations in δ and γ.

We target $U_T = X_{\pi/2}$, as it can be used to form a basis for single-qubit operations $\{X_{\pi/2}, Z_\theta\}$, with Z_θ implemented as virtual Z gates [56] for an arbitrary angle θ. We use the same pulse ansatz from Eq. (2) to obtain gates protected against different parameter deviations by adjusting the range of error values used in the cost function. We derive the FROG gate by setting $\gamma_{\min} = \gamma_{\max} = 0$ and $\delta/(2\pi) \in [-0.5, 0.5]$ MHz with $t_g = 112$ ns, and we derive the AROG gate by choosing $\gamma/(2\pi) \in [-1.2, 1.2]$ MHz and $\delta/(2\pi) \in [-0.25, 0.25]$ MHz with $t_g = 128$ ns. The pulse envelopes for FROG and AROG are shown in Figs. 1(b) and 1(c), respectively. Further details about the optimization method are provided in Appendix B. The open-source code is also available online [57].

To provide a baseline for comparison, we use a Gaussian pulse with DRAG corrections, as shown in Fig. 1(a). To ensure comparable exposure to noise relative to the robust gates, we choose a duration of 128 ns, although the DRAG gate could, in principle, be shorter. Robust gates typically require a larger pulse area because the control field must compensate for parameter variations, which demands additional rotations in the Hilbert space. Considering the pulse area

$$A = \int_0^{t_g} \left|\Omega_x(t) + i\Omega_y(t)\right| dt, \quad (5)$$

we obtain $A_{\mathrm{FROG}} \simeq 1.5\pi$, and $A_{\mathrm{AROG}} \simeq 2.1\pi$ for the robust gates, compared to $A_{\mathrm{DRAG}} \simeq 0.5\pi$ for DRAG. Under experimental amplitude constraints, set by the available power and attenuation, the FROG gate must be approximately three times longer and the AROG gate four times longer than the fastest available DRAG pulse.

C. Experimental validation

On the device, we first measure the performance of the gates with no added error using randomized-benchmarking (RB) experiments [58–60]. The error for all gates is comparable at $\mathcal{E}_{\mathrm{DRAG}} = 1.00(4) \times 10^{-3}$, $\mathcal{E}_{\mathrm{FROG}} = 0.94(4) \times 10^{-3}$, and $\mathcal{E}_{\mathrm{AROG}} = 1.08(3) \times 10^{-3}$. Details of the calibration to achieve these gate errors are presented in Appendix C.

To determine the gate error as a function of parameter deviations, we introduce static parameter offsets in the ranges $\delta/(2\pi) \in [-0.7, 0.7]$ MHz and $\gamma/(2\pi) \in [-3.5, 3.5]$ MHz. The parameter offsets are chosen such that they span around three times the respective ranges over which AROG is optimized and are sampled on a 21×21 grid. To efficiently explore a large parameter space, we take the RB sequence error at a single length $N_C = 60$, averaged over ten randomizations, as a proxy for the gate error [61]. The average gate fidelity F_g is approximately related to the average sequence fidelity F_{seq} at a single length N_C as

$$F_{\mathrm{seq}} \approx A\left(F_g\right)^{N_C N_g} + B, \quad (6)$$

where N_g refers to the average number of physical gates required to implement each Clifford gate, and A and B take into account state-preparation and measurement (SPAM) errors [62]. To implement Clifford gates using exclusively the optimized pulses, we choose a gate decomposition $\{X_{\pi/2}, -X_{\pi/2}, Y_{\pi/2}, -Y_{\pi/2}\}$, where Y rotations are obtained by applying the same pulse envelope as for X, but with the drive phase shifted by $\pm\pi/2$ relative to the X axis. The chosen decomposition results in $N_g = 2.25$. In full RB experiments, the parameters A and B are found by the fit to data. We work backward from the sequence fidelity, setting $A = 0.435$ and $B = 0.507$ according to our readout-characterization matrix, assuming similar behavior of the sequence fidelity F_{seq} as in the full RB measurements.

As the DRAG gate is not designed to compensate for parameter fluctuations, the sequence error $1 - F_{\mathrm{seq}}$ increases with amplitude errors γ and frequency errors δ, as shown in Fig. 1(d). The FROG gate expands the protected region along the detuning dimension but compresses it along the amplitude dimension, while the AROG gate adds amplitude protection without sacrificing robustness to static frequency noise. In experiment, the FROG gate maintains a sequence error $1 - F_{\mathrm{seq}}$ corresponding to a gate error $\mathcal{E}_g \leq 5 \times 10^{-3}$ (estimated from Eq. (6)) over 100% of the range targeted by its optimization, as shown in Fig. 1(e), compared to 37.5% for the DRAG and

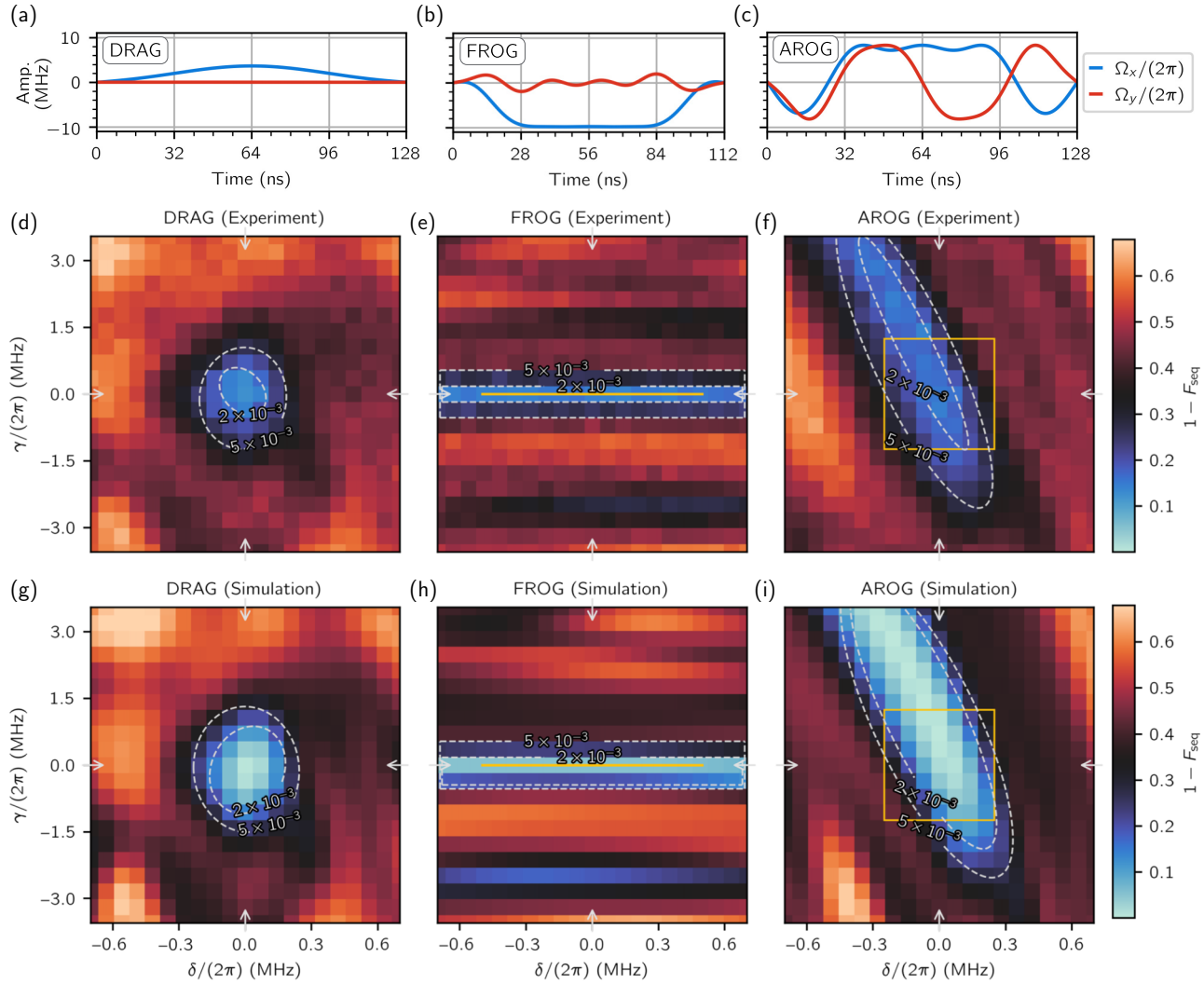


FIG. 1. Pulse envelopes for (a) DRAG, (b) FROG, and (c) AROG. The FROG and AROG pulses are given by Eq. (2). Randomized benchmarking sequence error $1 - F_{\text{seq}}$ at length $N_C = 60$ as a function of frequency error δ and amplitude error γ for the (d) DRAG, (e) FROG, and (f) AROG gates. Simulations of the three gates performed using Eq. (1) are shown in (g)–(i) for comparison. The color bar shows the sequence error, and the contour lines correspond to gate errors $\mathcal{E}_g = 2 \times 10^{-3}$ and $\mathcal{E}_g = 5 \times 10^{-3}$, estimated from the sequence error using Eq. (6). The yellow line and box indicate the range of errors over which FROG and AROG are optimized. The arrows indicate line cuts at zero amplitude error and at zero frequency error, with the corresponding line plots shown in Fig. 2.

AROG gates. We adopt $\mathcal{E}_g = 5 \times 10^{-3}$ as a threshold gate error throughout and note its relevance for QEC thresholds [9,63]. Over the rectangular region of parameter variations targeted in the AROG optimization, indicated by the yellow box in Fig. 1(f), the AROG gate has $\mathcal{E}_g \leq 5 \times 10^{-3}$ over 64.1% of the area, an improvement of 42.2% for the reference DRAG gate and 35.9% for the FROG gate. Both FROG and AROG also have low error $\mathcal{E}_g \leq 5 \times 10^{-3}$ outside the targeted parameter ranges. For the FROG gate, the protection is simply extended along the frequency-error axis, while the low error area for the AROG gate forms a tilted ellipse. This shape is an artifact of the optimization, and we address its implications further in the discussion. The experimental results are supported by simulations using the Hamiltonian in Eq. (1), with good agreement shown in Figs. 1(g)–1(i). All gates exhibit an increase in error of approximately 1×10^{-3} in experiment compared to simulation, due to decoherence and other noise not included in the model.

To further quantify the robustness of the gates, we fit a Gaussian to two line cuts, shown in Fig. 2, from the sequence error landscape. The line cuts are at zero frequency error and at zero amplitude error, for each gate, as indicated by the gray arrows in Fig. 1. The AROG gate adds amplitude protection, with $\mathcal{E}_g \leq 5 \times 10^{-3}$ over the range $\gamma/(2\pi) \in [-2.0, 1.7]$ MHz, compared to $[-1.2, 1.1]$ MHz for DRAG and $[-0.4, 0.4]$ MHz for FROG, as shown in Fig. 2(a). The amplitude protection does not

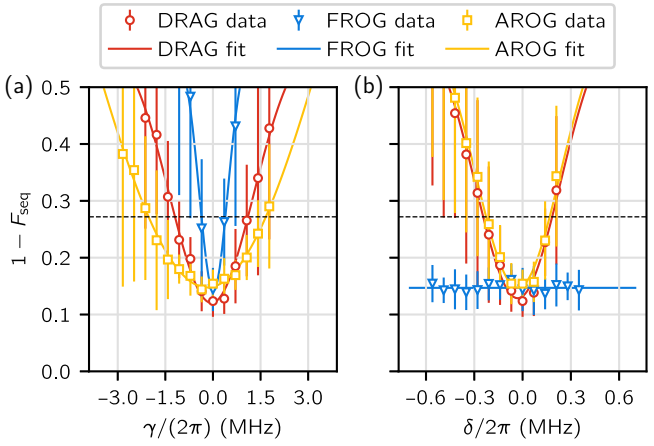


FIG. 2. Randomized benchmarking sequence error $1 - F_{\text{seq}}$ at length $N_C = 60$ for (a) amplitude errors γ and (b) frequency errors δ for the DRAG, FROG, and AROG gates. Each panel shows a line cut from the 2D plots shown in Fig. 1 along the directions indicated by the grey arrows. The error bars reflect the standard deviation across different randomizations. The data are fitted with Gaussian functions. The horizontal line indicates a gate error $\mathcal{E}_g = 5 \times 10^{-3}$, estimated from the sequence fidelity using Eq. (6).

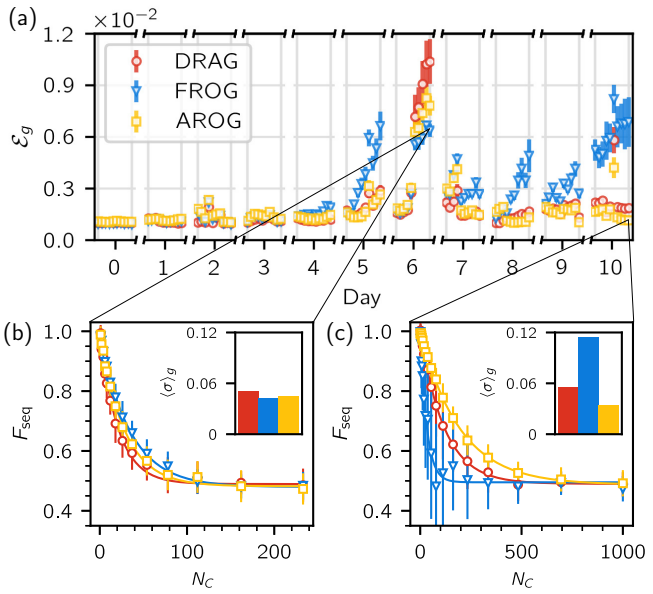


FIG. 3. (a) Gate error $\mathcal{E}_g$ for the DRAG, FROG, and AROG gates, extracted from RB experiments for 10 h each day over 11 days. RB curves for (b) day 6 and (c) day 10 are connected by lines to time points of interest in (a). The error bars at each sequence length N_C reflect the standard deviation across different randomizations, and the insets show the mean standard deviation $\langle\sigma\rangle_g$ over all sequence lengths.

compromise robustness to static frequency noise for the AROG gate, which remains comparable to that of a DRAG gate; both achieve $\mathcal{E}_g \leq 5 \times 10^{-3}$ over $\delta/(2\pi) = \pm 0.2$ MHz. The FROG gate has sequence error corresponding to $\mathcal{E}_g \leq 5 \times 10^{-3}$ over the full measured frequency range $\delta/(2\pi) = \pm 0.7$ MHz, as can be seen in Fig. 2(b).

III. PARAMETER FLUCTUATIONS OVER TIME

To understand when robustness is beneficial in realistic noise environments, we further investigate gate performance as the parameters fluctuate over time. We track amplitude and frequency errors, as well as qubit coherence times, over 11 days. We measure amplitude deviations γ with an error-amplification sequence $X_{\pi/2}^{(2n+1)}$. The final population is fitted to a cosine as a function of the number of repetitions n [64], as described in detail in Appendix C. We measure the qubit frequency drift δ and dephasing time T_2^* from Ramsey experiments for various delays τ_r. The T_1 value is extracted from a decay experiment in which the qubit is excited and the remaining population is measured after delays τ_d. The pure dephasing time T_ϕ can be calculated from these measurements using the relation $1/T_\phi = (1/T_2^*) - (1/2T_1)$. To ensure that the measured quantities reflect the same noise environment on average, the experiments are interleaved on a shot-by-shot basis: a new set (n, τ_r, τ_d) of amplitude-error repetitions n, Ramsey delay time τ_r, and T_1 delay time τ_d is measured in each experiment (each shot). In this manner, we simultaneously iterate over $n \in \{0, \ldots, 34\}$, $\tau_r \in [0, 40]$ µs, and $\tau_d \in [1\text{ ns}, 100\text{ µs}]$, each discretized into 35 points. Having iterated through all 35 sets of (n, τ_r, τ_d), we repeat this sequence 2^{12} times. The full characterization measurement is repeated ten times, which takes approximately 10 min.

To determine how the parameter fluctuations affect gate error, we perform RB experiments between the full characterization measurements. The DRAG, FROG, and AROG gate performance is measured by interleaving data points across randomizations, ensuring that each gate is sampled uniformly over the parameter drifts. Each RB experiment contains $N_r = 60$ randomizations and $N_s = 16$ sequence lengths for each gate. Averaging over 2^8 repetitions, the full measurement runs for approximately 30 min. The cycle of characterization and RB is repeated continuously for 10 h per day over 11 consecutive days.

The gate error $\mathcal{E}_g$ stays relatively stable for all gates in the first 5 days but fluctuates thereafter, with increases by as much as $9(1) \times 10^{-3}$ on day 6 and $7.3(8) \times 10^{-3}$ on day 10, as shown in Fig. 3(a). The different pulses exhibit varying levels of robustness on these days, as shown by their RB performance, depicted in Figs. 3(b) and 3(c), respectively. In what follows, we examine the parameter fluctuations in detail and analyze how they contribute to the observed variations in gate error, with particular attention to day 6, where the qubit experienced strong dephasing, and day 10, where large amplitude errors occurred.

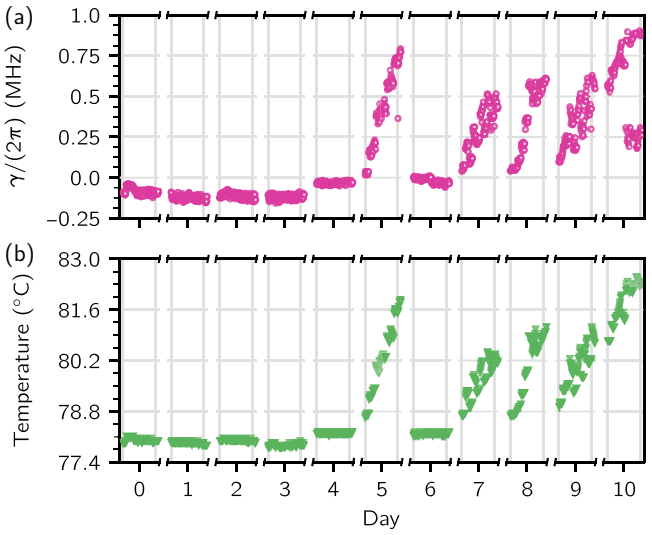


FIG. 4. (a) Amplitude error γ for an $X_{\pi/2}$ gate extracted from error-amplification experiments and (b) internal temperature for the device used to generate the drive signals, measured independently for 10 h each day for 11 days.

A. Amplitude drifts

Over the 11 days of measurement, we observe gradual drive-amplitude drifts by over $\gamma/(2\pi) = 0.90$ MHz (6%) from the initial calibrated value, with the slow drift accompanied by smaller, short-term fluctuations. These drifts occur on specific measurement days (day 5 and days 7–10), whereas on other days (days 0–4 and day 6), the amplitude deviations remain almost constant near zero, as shown in Fig. 4. We attribute amplitude drifts mainly to temperature instabilities on the control device. The amplitude deviations have a Pearson correlation of $r = 0.94$ (95% CI: 0.933–0.946) with the internal temperature of the device used to generate the drive signal, shown in Fig. 4(b). The effects of these drifts are evident in the changes in gate error $\mathcal{E}_g$ over time. The FROG gate, which has increased sensitivity to amplitude deviations, experiences increased gate errors caused by the drifts on days 5 and 7–10, as shown in Fig. 3(a).

Although less affected by these events, the DRAG and AROG gates still exhibit increased error. Day 10 provides a clear example of this effect: the amplitude deviates by $\gamma/(2\pi) = 0.88$ MHz as the device heats up by nearly 5 °C. Consequently, the DRAG gate error increases by 87.9% from the initial calibration with $\Delta\mathcal{E}_{\mathrm{DRAG}} = 8.8(9) \times 10^{-4}$. In contrast, the AROG gate error increases by only 5.4% with $\Delta\mathcal{E}_{\mathrm{AROG}} = 6(5) \times 10^{-5}$, corresponding to a 15-fold improvement over DRAG in added error, as shown in Fig. 3(c). The effect of amplitude errors is also captured by the spread of the RB, which increases in the presence of coherent errors [65]. Before the amplitude drift, all gates show a mean standard deviation over sequence lengths of $\langle\sigma\rangle_g = 0.03$. During the drift, the spread increases substantially

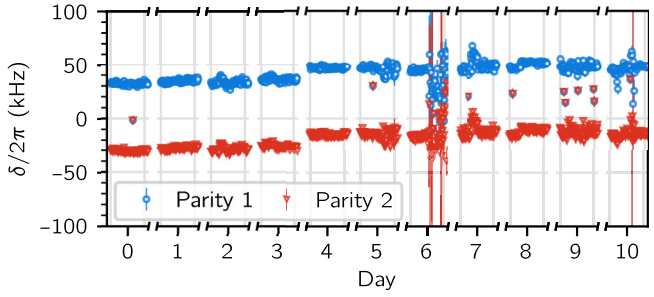


FIG. 5. Qubit frequency extracted from Ramsey experiments for 10 h each day in an 11-day period. The two distinct frequency regions indicate the even (blue circle) and odd (red triangle) parity states of the qubit.

for the FROG gate, reaching $\langle\sigma\rangle_{\mathrm{FROG}} = 0.11$, and it doubles for the DRAG gate to $\langle\sigma\rangle_{\mathrm{DRAG}} = 0.06$, whereas the AROG gate maintains the same value of $\langle\sigma\rangle_{\mathrm{AROG}} = 0.03$, as shown in the inset of Fig. 3(c).

B. Frequency drifts

We observe qubit frequency drifts of up to $\delta = 77(3)$ kHz over the 11-day period, well within the protected area for all three gates, as shown in Fig. 5. The frequency measurement is imprecise on day 6, and at some points on day 10, due to low qubit coherence, which we discuss in the next section. The qubit exhibits two distinct frequencies, which can be attributed to quasiparticle-induced charge-parity switching [14]. The difference between frequencies remains stable around 61.4(4) kHz. Compared to the effect of other parameters, the small quasistatic drifts in qubit frequency do not compromise gate performance; however, charge-parity switching also contributes to qubit dephasing [14], the effect of which on gate error we address next.

C. Coherence time drifts

The pure dephasing time T_ϕ and decay time T_1 vary from 1 to 26 μs and from 11 to 80 μs, respectively. The fluctuations are largest on days 6–7 and 9–10, as shown in Fig. 6. On these days, the two time series have a Pearson correlation greater than $r = 0.325$, which we choose as a threshold for meaningful correlation because it corresponds to a statistically significant p value of 0.001 for our measurements of 100 data points per day. The correlations suggest a common source of noise affecting both relaxation and dephasing. The T_ϕ time reflects random fast frequency fluctuations beyond the quasistatic noise captured by the central frequency drift, and we observe resilience to this stochastic noise by the robust gates, particularly FROG.

The lowest qubit coherence occurs on day 6, with reduced T_1 and T_ϕ for a period of around 6 h. The gates experience an increase in error of $\Delta\mathcal{E}_{\mathrm{FROG}} = 5.7(3) \times 10^{-3}$, $\Delta\mathcal{E}_{\mathrm{AROG}} = 7.2(6) \times 10^{-3}$, and $\Delta\mathcal{E}_{\mathrm{DRAG}} = 9(1) \times 10^{-3}$ from the initial calibrated values. Operating with a

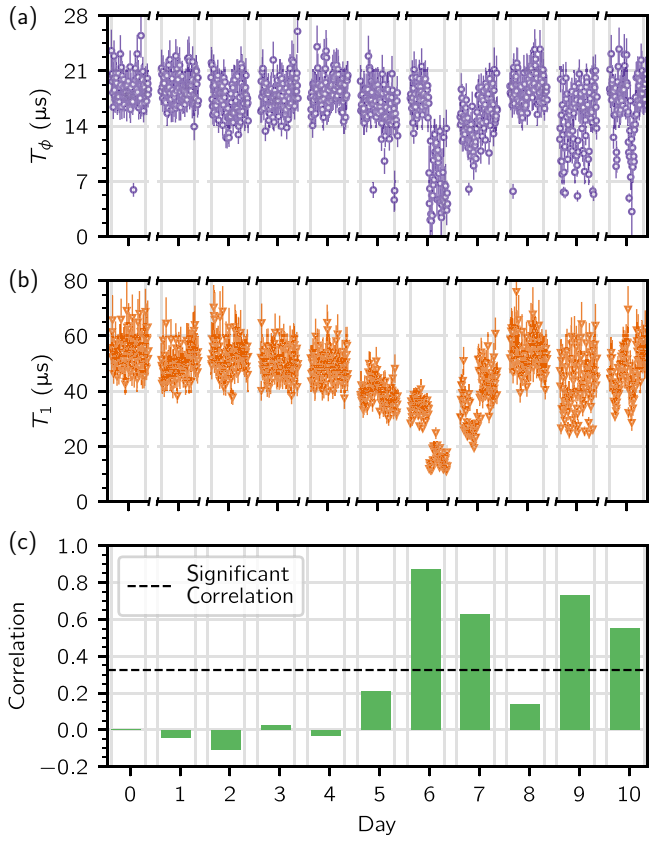


FIG. 6. (a) Qubit pure dephasing time T_ϕ and (b) qubit decay time T_1 extracted from Ramsey and decay experiments interleaved on a shot-by-shot basis for 10 h each day in an 11-day period. (c) Pearson correlation between T_ϕ and T_1 each day. The dashed horizontal line indicates a correlation of 0.325 ($p = 0.001$).

FROG gate leads to a 1.6-fold reduction in additional error, and with AROG to a 1.3-fold reduction, during the period of low qubit coherence, as shown by the RB curves in Fig. 3(b). During another reduction in T_ϕ on day 10, lasting around an hour, the DRAG gate error again rises above 5×10^{-3}, with an increase of $\Delta\mathcal{E}_{\mathrm{DRAG}} = 4.8(8) \times 10^{-3}$ over the day-0 value. This time, the AROG gate shows an increase of $\Delta\mathcal{E}_{\mathrm{AROG}} = 3.1(8) \times 10^{-3}$, 1.5 times less additional error than the DRAG gate, while we observe an increase in the FROG gate error by $\Delta\mathcal{E}_{\mathrm{FROG}} = 7.3(8) \times 10^{-3}$, mainly due to a simultaneous amplitude drift of $\gamma/(2\pi) = 0.83$ MHz. A more detailed analysis is required to disentangle the individual contributions of the parameter fluctuations to the observed gate error.

D. Sensitivity analysis

To quantify the change in gate error per parameter, we perform a ridge regression on the time-series data. The regression evaluates the sensitivity $\Delta\mathcal{E}_g/\Delta x$ with respect to $x = \gamma^2, \Gamma_\phi, \Gamma_1$ for each gate pulse, i.e., $g =$ DRAG, FROG, AROG. We use the square of the amplitude error γ^2, due to the expected relationship with gate error $1 - F_g \propto \gamma^2$, and we omit qubit frequency drifts δ, which have negligible effects in our experiments. We use the rates $\Gamma_\phi = 1/T_\phi, \Gamma_1 = 1/T_1$ rather than coherence times to capture their nonlinear relationship with gate error. At each time point, we have a vector $\mathbf{x}_k = ((\gamma^2)^k, \Gamma_\phi^k, \Gamma_1^k) \in \mathbb{R}^3$ of inputs, which the regression maps to an output $\boldsymbol{\mathcal{E}}_k = (\mathcal{E}^k_{\mathrm{DRAG}}, \mathcal{E}^k_{\mathrm{FROG}}, \mathcal{E}^k_{\mathrm{AROG}}) \in \mathbb{R}^3$, consisting of the error for each gate. Before fitting, we normalize the parameters as $\tilde{\mathbf{x}}_k = (\mathbf{x}_k - \boldsymbol{\mu})/\boldsymbol{\sigma}$, using the mean $\boldsymbol{\mu} = (\mu_{\gamma^2}, \mu_{\Gamma_\phi}, \mu_{\Gamma_1})$ and standard deviation $\boldsymbol{\sigma} = (\sigma_{\gamma^2}, \sigma_{\Gamma_\phi}, \sigma_{\Gamma_1})$ of each parameter over time. The ridge regression minimizes the mean-squared error,

$$\frac{1}{m}\sum_{k=1}^{m}\left(\boldsymbol{\mathcal{E}}_k - \tilde{\mathbf{x}}_k^\top \tilde{\mathbf{w}}\right)^2 + \boldsymbol{\lambda}\|\tilde{\mathbf{w}}\|_2^2, \tag{7}$$

where $m = 110$ is the number of samples and $\tilde{\mathbf{w}} \in \mathbb{R}^9$ is the weight vector to be fitted, which quantifies the change in error per change in normalized parameter $\tilde{w}_{x,g} = \Delta\mathcal{E}_g/\Delta\tilde{x}$. To obtain the coefficients in physical units, the regression weights $\tilde{\mathbf{w}}$ (fitted on normalized features $\tilde{\mathbf{x}}$) are rescaled by the corresponding normalization factors to give the sensitivities $w_{x,g} = \tilde{w}_{x,g}/\sigma_x = \Delta\mathcal{E}_g/\Delta x$ for each parameter x and gate g. The final fit for all gates has an R^2 value of 0.71, where we impose $\boldsymbol{\lambda} \geq 0$ for regularization to avoid overfitting and to keep the sensitivities within a physically meaningful range. The sensitivities in physical units are listed in Table I.

TABLE I. Scaled weights from a ridge-regression model for three parameters: amplitude deviation squared γ^2, dephasing rate Γ_ϕ, and relaxation rate Γ_1. The values represent the change in gate error per parameter $w_x = \Delta\mathcal{E}/\Delta x$ and are fitted for DRAG, FROG, and AROG gates.

	w_{γ^2} (10^{-2} MHz^{-2})	w_{Γ_ϕ} (10^{-2} MHz^{-1})	w_{Γ_1} (10^{-2} MHz^{-1})
DRAG	0.26	3.87	4.28
FROG	2.24	2.30	3.72
AROG	≈0	2.74	4.27

To verify the physical relevance of the fit, we compare the sensitivity to decay w_{Γ_1} to an analytical formula for coherence limits. From the relationship $\mathcal{E}_g \approx (t_g/3)\Gamma_1$ [60], we calculate $w_{\Gamma_1}^{\mathrm{analytical}} = 4.27 \times 10^{-2}$ MHz^{-1} for DRAG and AROG and $w_{\Gamma_1}^{\mathrm{analytical}} = 3.73 \times 10^{-2}$ MHz^{-1} for FROG, a near match in all cases. As expected from our design and initial experiments, the FROG gate shows a pronounced sensitivity to amplitude errors, while the DRAG gate is an order of magnitude less sensitive and the AROG gate exhibits no dependence within the range of the observed drifts. Additionally, the FROG and AROG gates are less sensitive to dephasing than the DRAG gate,

with the FROG gate about 1.7 times and the AROG gate about 1.4 times more robust, illustrating how robustness to static frequency errors can also add protection during fluctuations in T_ϕ.

IV. DISCUSSION AND CONCLUSION

We have demonstrated the effectiveness of robust single-qubit gates in maintaining stable gate operations, both during quasistatic parameter mismatches and stochastic time-dependent errors. Using a gradient-based numerical optimization method, we generated a frequency-robust gate that has protection against detuning errors, and an amplitude-and-frequency-robust gate that is robust against amplitude errors without sacrificing protection against frequency errors. Under controlled static variations of detuning and amplitude, the FROG and AROG pulses maintain gate errors below 5×10^{-3} for parameter deviations up to three times larger than those tolerated by DRAG. The convergence of the RB measurements in experiments also indicates no significant leakage compared to DRAG, which is achieved by including the third level in the optimization Hamiltonian. Indeed, we verify in simulations that, for all parameter deviations, the $|2\rangle$-state population after applying the gate to the ground state satisfies $p(|2\rangle) \leq 1.4 \times 10^{-8}$ for FROG and $p(|2\rangle) \leq 1.0 \times 10^{-6}$ for AROG.

We further relate fluctuations in drive amplitude, qubit frequency, and coherence times to the gate error of the different pulse designs over time. During the largest amplitude drift on day 10, the AROG gate experienced over 15 times less added error than the DRAG gate. Additionally, RB revealed a narrower distribution of sequence fidelity for the AROG gate compared to the DRAG gate during this drift. The broader spread across randomizations in the DRAG gate benchmarking data indicates larger coherent errors, which lead to a higher worst-case error rate [65]. This is particularly relevant for fault-tolerant quantum computing, where the worst-case error plays a critical role in determining whether the threshold of QEC codes will be met [3,9,10]. We trace the amplitude deviations back to temperature variations of the control device, with fluctuations as large as 1% per degree Celsius. Temperature changes in the laboratory, heating of other equipment, and internal heating of the device can all contribute. When errors in classical control hardware cause drifts, a processor using AROG gates can continue operating without recalibration.

Although the gates are optimized to suppress coherent errors, previous simulations suggest that robust designs could also provide resilience to stochastic errors such as fast frequency fluctuations from TLSs [24,28,38]. We experimentally confirm this effect for the FROG and AROG gates, which experienced smaller fidelity losses than DRAG during periods of high dephasing, with up to 1.7 times and 1.5 times less added gate error, respectively. The reductions in T_ϕ were correlated with reductions in T_1 and occurred on minute-to-hour time scales, which is consistent with prior reports on TLS-induced noise signatures [7,15,16,18,19,21,66]. The robustness has practical implications for the operation of superconducting processors. Advances in shielding, design, and fabrication have reduced the density and coupling of TLS defects [67–75], and *in situ* control strategies to actively suppress TLS noise have also been proposed [76–83], but strongly coupled TLSs and spatiotemporal correlations remain a major error source [84,85]. In the presence of stochastic frequency-related noise—including from TLSs, which are difficult to avoid, control, or mitigate in other ways—robust gates may provide sufficient resilience to preserve computational usefulness.

Future work involves building on our understanding of gate performance and noise effects to further harness the potential of the gradient-based optimization method and the resulting robust gates introduced here. Both FROG and AROG exhibit regions of low error extending beyond the parameter ranges explicitly defined in their optimization cost functions, as can be seen in Fig. 1. For the FROG gate, this low-error extension follows the targeted frequency-error axis, while for AROG, it forms a tilted elliptical region in the amplitude-frequency plane, indicating a dependence of the two principle components. Such a dependence is advantageous only when amplitude and frequency errors are correlated, which we do not observe in our experiments. The dependence is not systematic and only occurs for some pulse-parameter initializations; it could be a result of the Fourier-pulse ansatz in Eq. (2), which consists of both odd harmonics (antisymmetric about the gate midpoint) and even harmonics (symmetric). Alternative cost functions could yield pulse designs with improved robustness characteristics. For example, incorporating weighted averages over the target parameter ranges or explicitly accounting for cross-sensitivities in the cost function could suppress unwanted tilting and concentrate robustness where it is most beneficial. Moreover, the same optimization framework could be extended to explicitly target stochastic noise processes. By integrating models of fast frequency fluctuations into the optimization on top of the static variations used in this work, subsequent pulse designs could further enhance the protection against stochastic noise already demonstrated by the FROG and AROG gates. In practice, increased robustness can lead to larger pulse areas, requiring high drive amplitudes for short pulses, motivating additional closed-loop optimization to mitigate pulse distortions [46,86] and achieve faster, higher-fidelity gates. Future implementations could combine robust pulse designs and classical stabilization of control hardware, tailoring the balance between frequency and amplitude robustness to each system's dominant noise sources. This hybrid strategy would

maximize performance while minimizing calibration overhead.

ACKNOWLEDGMENTS

We acknowledge financial support from the German Federal Ministry of Education and Research via the funding program *Quantum Technologies—From Basic Research to the Market* under Contracts No. 13N15680 *GeQCoS* and No. 13N16188 *MUNIQC-SC*; the Deutsche Forschungsgemeinschaft (DFG, German Research Foundation) via Project No. FI2549/1-1 and Germany's Excellence Strategy EXC-2111-390814868 *MCQST*; and the European Union's Horizon research and innovation program through the projects *OpenSuperQPlus100* (Grant No. 955479) and *MOlecular Quantum Simulations (MOQS)* (Grant No. 955479). We also acknowledge support from the EU MSCA Cofund *International, Interdisciplinary, and Intersectoral Doctoral Program in Quantum Science and Technologies (QUSTEC)* (Grant No. 847471). This research is part of the *Munich Quantum Valley*, supported by the Bavarian state government with funds from the Hightech Agenda Bayern Plus. Emily Wright acknowledges support from the *International Max Planck Research School for Quantum Science and Technology (IMPRS-QST)*.

DATA AVAILABILITY

The data that support the findings of this article are not publicly available upon publication because it is not technically feasible and/or the cost of preparing, depositing, and hosting the data would be prohibitive within the terms of this research project. The data are available from the authors upon reasonable request.

APPENDIX A: EXPERIMENTAL SETUP

Our experiments are performed on one qubit from a pair of transmon-type fixed-frequency superconducting qubits [53] coupled by a flux-tunable coupler [87,88]. The qubits are controlled and measured using a Super High Frequency Qubit Controller (SHFQC) from Zurich Instruments. A schematic of the experimental setup is shown in Fig. 7. We use charge-coupled direct drive lines on the chip for qubit control. The readout resonators are coupled to a common feedline. The feedline is attenuated by -80 dB distributed over the temperature stages and filtered with a 5.5-GHz high-pass filter (VHF-5050+). The drive lines are attenuated by -60 dB distributed over the different temperature stages and filtered with a 3.5–4.5-GHz band-pass filter (VBFZ-4000-S+). We use two 4–12-GHz isolators on the output line. The output signal is amplified by a 4–8-GHz 40-dB high-electron-mobility (HEMT) cryogenic low-noise amplifier (LNF-LNC4 8G) thermalized at the 3-K stage. The signal is amplified by a 40-dB low-noise room-temperature amplifier (DBLNA104000800A) before being digitized at the SHFQC input. The flux is controlled using a Zurich Instruments high-density, multichannel arbitrary-waveform generator (HDAWG). The flux line is attenuated at room temperature by -10 dB and by -20 dB at the 3-K stage and filtered using a 1.35-GHz low-pass filter (VLFX-1350+). We select the qubit with higher coherence times and we bias the tunable coupler at its sweet spot.

APPENDIX B: OPTIMIZATION ALGORITHM

1. Cost function

We use the cost function described in Eq. (4) of the main text. To prevent excessively large pulse amplitudes, we impose constraints of the form

$$\begin{aligned} -\eta\Omega_0 \le \Omega_x \le \eta\Omega_0, \\ -\eta\Omega_0 \le \Omega_y \le \eta\Omega_0, \end{aligned} \tag{B1}$$

where $\eta = 0.55$ for the FROG pulse and $\eta = 0.46$ for the AROG pulse. In experiment, the maximum absolute drive amplitudes to implement an $X_{\pi/2}$ rotation are 3.6, 9.8, and 8.2 MHz for DRAG, FROG, and AROG, respectively.

2. Time evolution

The time-evolution operator $U_{ij}(t_g)$ in the cost function is obtained by numerically simulating the system dynamics for each parameter pair (δ_i, γ_j). The total gate time t_g is discretized into N time steps such that $t_g = N\Delta t$. The control pulse is assumed to be piecewise constant over each interval, allowing the Hamiltonian to be treated as time independent within each step. At each time step n, the propagator is given by $P_{ij,n} = \exp(-iH_{ij,n}\Delta t)$, where $H_{ij,n}$ is the Hamiltonian at that interval under parameter deviations (δ_i, γ_j) defined in Eq. (1) of the main text. The full time-evolution operator is then constructed by sequentially multiplying these propagators:

$$U_{ij}(t_g) = P_{ij,N}P_{ij,N-1}\cdots P_{ij,1}.$$

3. GRAPE for analytically shaped pulses

To perform the GRAPE optimization, we require the gradients of the cost function with respect to the control functions, specifically $\partial J/\partial\Omega_{x,n}$ and $\partial J/\partial\Omega_{y,n}$ at each time step t_n. These gradients guide the update of the control fields to minimize the cost function J. For details of the gradient-calculation methods used in GRAPE, we refer the

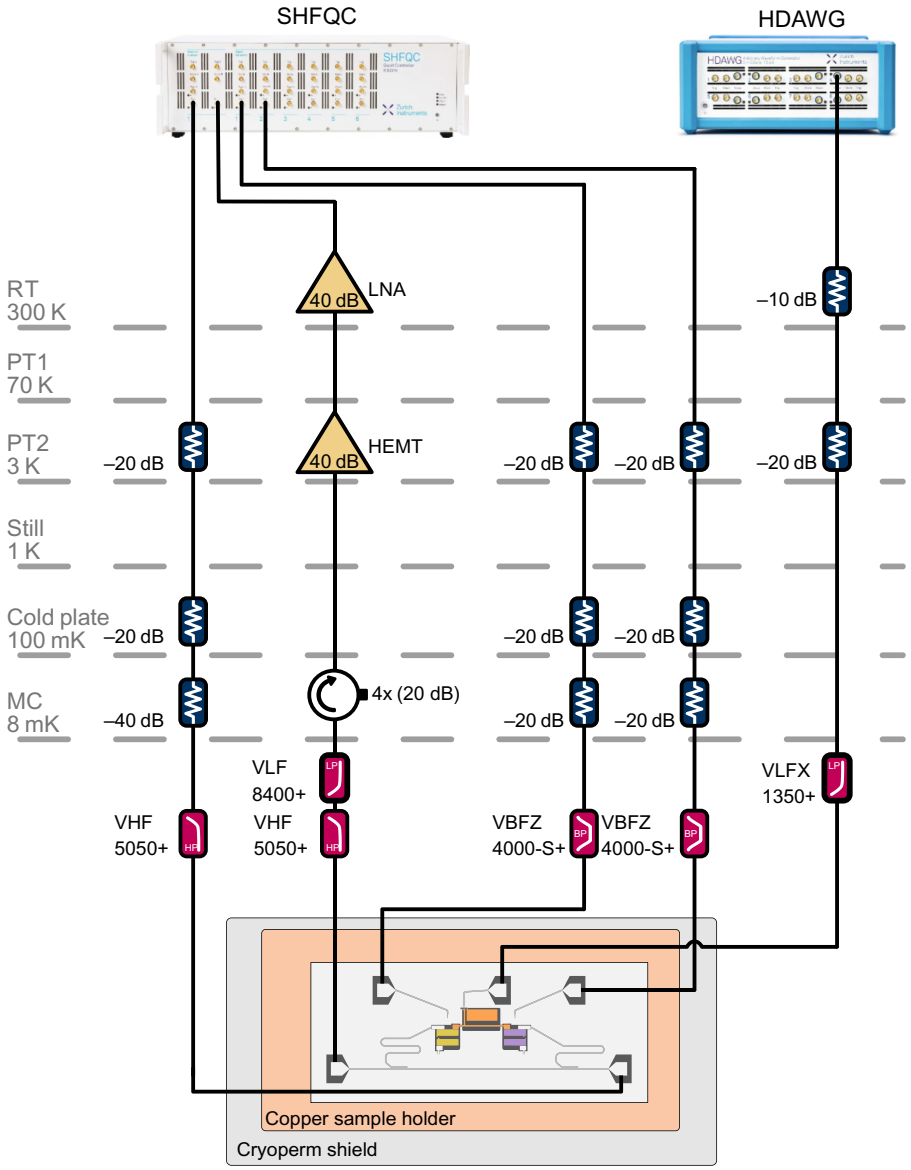


FIG. 7. Experimental setup and schematic of the wiring for the superconducting qubit experiment. The qubits are highlighted in yellow and purple, and the tunable coupler is colored orange in the schematic of the chip.

reader to Refs. [48,49,89]. In our case, we have

$$\frac{\partial J}{\partial \Omega_{x,n}} = \frac{1}{N_\delta N_\gamma} \sum_{i,j} \left(1 + \frac{\gamma_j}{\Omega_0}\right) \mathbb{R}\left[\mathrm{Tr}\left(V^\dagger_{ij,n} X_{ij,n} U_{ij,n}\right)\right],$$

$$\frac{\partial J}{\partial \Omega_{y,n}} = \frac{1}{N_\delta N_\gamma} \sum_{i,j} \left(1 + \frac{\gamma_j}{\Omega_0}\right) \mathbb{R}\left[\mathrm{Tr}\left(V^\dagger_{ij,n} Y_{ij,n} U_{ij,n}\right)\right],$$

where

(a) $U_{ij,n} = P_{ij,n} P_{ij,n-1} \cdots P_{ij,1}$,

(b) $V^\dagger_{ij,n} = V^\dagger_{ij,N} P_{ij,N} \cdots P_{ij,n}$, with

$$V_{ij,N} = -\tfrac{1}{2} U_\mathrm{T} \left(|0\rangle\langle 0| + |1\rangle\langle 1|\right) \times \left(\langle 0| U^\dagger_\mathrm{T} U_{ij}(t_g) |0\rangle + \langle 1| U^\dagger_\mathrm{T} U_{ij}(t_g) |1\rangle\right),$$

(c) $X_{ij,n} = -i(\Delta t/2)\left(\hat{\sigma}^x_{10} + \hat{\sigma}^x_{21}\right) - (\Delta t^2/4)[H_{ij,n}, \hat{\sigma}^x_{10} + \hat{\sigma}^x_{21}] + O(\Delta t^3)$,

(d) $Y_{ij,n} = -i(\Delta t/2)\left(\hat{\sigma}^y_{10} + \hat{\sigma}^y_{21}\right) - (\Delta t^2/4)[H_{ij,n}, \hat{\sigma}^y_{10} + \hat{\sigma}^y_{21}] + O(\Delta t^3)$.

In our approach, the control pulse is not optimized directly at each time step. Instead, it is decomposed into a Fourier series, as defined in Eq. (2), and the optimization

is performed over the corresponding Fourier coefficients a_n and b_n, which determine the pulse shape. Consequently, we require the gradients $\partial J/\partial a_n$ and $\partial J/\partial b_n$, which can be computed using the chain rule [55]:

$$\frac{\partial J}{\partial a_n} = \frac{\partial J}{\partial \Omega_{x,n}}\frac{\partial \Omega_{x,n}}{\partial a_n} + \frac{\partial J}{\partial \Omega_{y,n}}\frac{\partial \Omega_{y,n}}{\partial a_n},$$
$$\frac{\partial J}{\partial b_n} = \frac{\partial J}{\partial \Omega_{x,n}}\frac{\partial \Omega_{x,n}}{\partial b_n} + \frac{\partial J}{\partial \Omega_{y,n}}\frac{\partial \Omega_{y,n}}{\partial b_n}.$$

The gradients of the constraints in Eq. (B1), which may be provided to the optimization routine to speed up the computation, are also obtained via this chain rule.

Once the cost function and its gradients are known, any standard optimization routine can be used to search for the set of parameters a_n and b_n that minimize the cost function in Eq. (4). Examples of such routines are `fmincon` in MATLAB or `scipy.optimize.minimize` in PYTHON.

4. Results

In this work, we design pulses that implement robust $X_{\pi/2}$ gates by setting the target unitary to

$$U_{\mathrm{T}} = \begin{pmatrix} \frac{1}{\sqrt{2}} & -\frac{i}{\sqrt{2}} & 0 \\ -\frac{i}{\sqrt{2}} & \frac{1}{\sqrt{2}} & 0 \\ 0 & 0 & 1 \end{pmatrix}.$$

TABLE II. Fourier coefficients of the optimal pulses. The pulses are given by Eq. (2).

FROG		AROG	
$a_1 = -0.6137$	$b_1 = -0.0106$	$a_1 = 0.3492$	$b_1 = 0.0859$
$a_2 = -0.0247$	$b_2 = 0.0334$	$a_2 = -0.2470$	$b_2 = -0.4581$
$a_3 = 0.0742$	$b_3 = 0.0579$	$a_3 = -0.2474$	$b_3 = -0.0206$
$a_4 = 0.0507$	$b_4 = 0.0140$	$a_4 = -0.0773$	$b_4 = 0.0213$
$a_5 = 0.0149$	$b_5 = -0.0416$	$a_5 = 0.0352$	$b_5 = 0.0614$

To account for leakage effects in the simulations, the system includes the lowest three energy levels. In all cases, we use a time step of $\Delta t = 0.5$ ns, which corresponds to the sampling time of the arbitrary-waveform generator (AWG).

For the FROG pulse, we choose $N = 224$ time steps, resulting in a total pulse duration of $t_g = 112$ ns. The pulse is optimized over a range of detunings $\delta/(2\pi) \in [-0.5, 0.5]$ MHz, discretized into $N_\delta = 21$ values. The amplitude scaling factor is fixed at $\gamma = 0$, with $N_\gamma = 1$. The AROG pulse is designed with $N = 256$ time steps, corresponding to a total duration of $t_g = 128$ ns. It is optimized over a range of detunings $\delta/(2\pi) \in [-0.25, 0.25]$ MHz and amplitude error $\gamma/(2\pi) \in [-1.2, 1.2]$ MHz, with $N_\delta = N_\gamma = 21$ discrete values. The resulting pulse coefficients are given in Table II, and the pulse envelopes are shown in Figs. 1(b) and 1(c) in the main text.

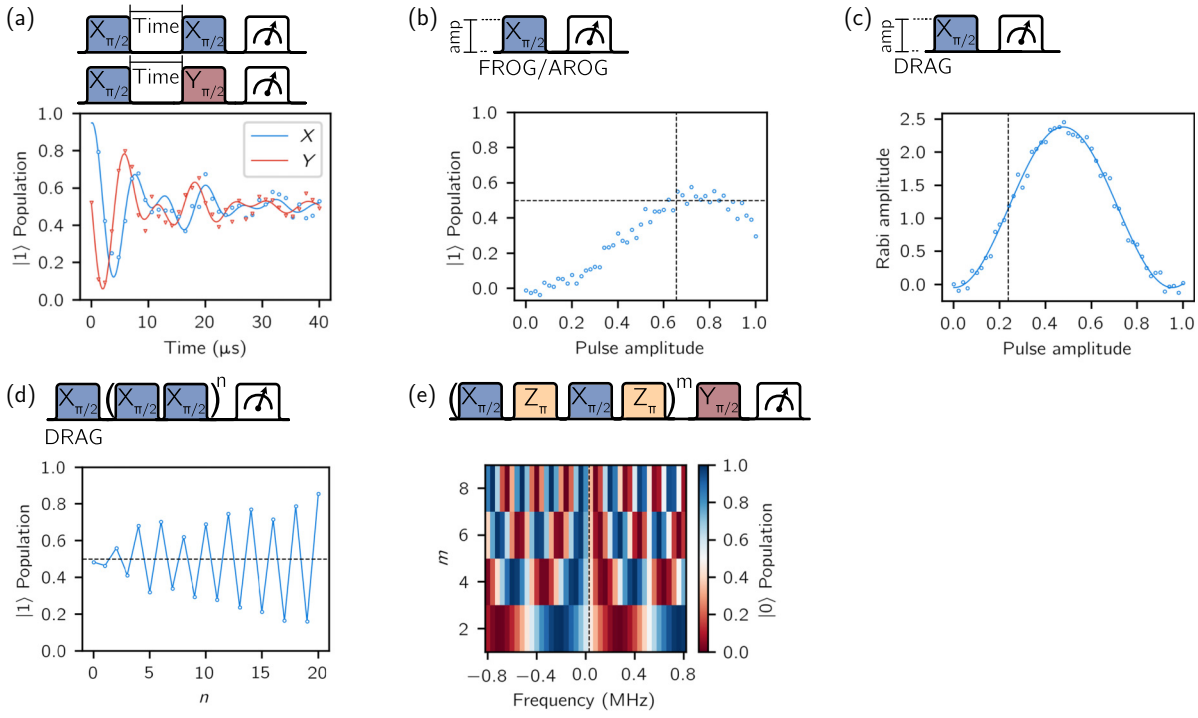


FIG. 8. Tune-up routine for single-qubit gates. (a) The qubit frequency is calibrated using a Ramsey experiment. The (b) FROG and AROG and (c) DRAG gates are then calibrated with a simple amplitude sweep. Subsequently, the DRAG gate is fine-calibrated using error-amplification sequences for the (d) pulse amplitude and (e) frequency and DRAG parameter.

APPENDIX C: GATE CALIBRATION

Each pulse parameter is calibrated sequentially to fully tune-up the gates. We first characterize the qubit frequency ω_{01} using a Ramsey pulse sequence [see Fig. 8(a)]. Due to charge-parity switching, we see two frequencies, leading to a beating pattern. We take the qubit frequency ω_{01} to be the average of these two frequencies.

We proceed to sweep the pulse amplitude for all gates until the desired population is reached. An $X_{\pi/2}$ pulse is realized when the population reaches 0.5, as shown in Fig. 8(b) for FROG and AROG and in Fig. 8(c) for DRAG. Note that the qubit rotation angle does not change linearly with the pulse amplitude for the robust gates, and the desired population lies on a small plateau.

For the DRAG gate, we perform additional tuning with fine amplitude targeting and simultaneous precise calibrations of the drive frequency and the DRAG correction parameter. Error-amplification sequences are performed to iteratively fine-tune each pulse parameter. For amplitude, the sequence $(X_{\pi/2})^{2n+1}$ is measured, as shown in Fig. 8(d). The final population is fitted to

$$P(|0\rangle) = a + \frac{1}{2}(-1)^n \cos\left(\frac{\pi}{2} + n\pi\frac{\gamma}{\Omega_0}\right) \tag{C1}$$

as a function of the number of repetitions n, where a is left as a fitting parameter, which goes to $1/2$ for a perfect $X_{\pi/2}$ gate, and γ is the amplitude error as defined in Eq. (1) [64]. The qubit undergoes a drive-induced frequency shift, which we also calibrate for the DRAG gate. The frequency is fine-tuned using the sequence $(X_{\pi/2}Z_{\pi}X_{\pi/2}Z_{\pi})^m Y_{\pi/2}$ for various m [64] [see Fig. 8(f)]. The DRAG parameter β in

$$\Omega(t) = \Omega_x(t) + i\beta\dot{\Omega}_x(t) \tag{C2}$$

is tuned using the same sequence, after the frequency-offset calibration.

[1] S. Krinner, N. Lacroix, A. Remm, A. Di Paolo, E. Genois, C. Leroux, C. Hellings, S. Lazar, F. Swiadek, J. Herrmann *et al.*, Realizing repeated quantum error correction in a distance-three surface code, Nature **605**, 669 (2022).

[2] Google Quantum AI, Suppressing quantum errors by scaling a surface code logical qubit, Nature **614**, 676 (2023).

[3] E. Knill, R. Laflamme, and W. H. Zurek, Resilient quantum computation: Error models and thresholds, Proc. R. Soc. Lond. A **454**, 365 (1998).

[4] R. Acharya, D. A. Abanin, L. Aghababaie-Beni, I. Aleiner, T. I. Andersen, M. Ansmann, F. Arute, K. Arya, A. Asfaw, N. Astrakhantsev *et al.*, Quantum error correction below the surface code threshold, Nature **638**, 920 (2025).

[5] V. Sivak, A. Morvan, M. Broughton, M. Neeley, A. Eickbusch, D. Abanin, A. Abbas, R. Acharya, L. A. Beni, G. Aigeldinger *et al.*, Reinforcement learning control of quantum error correction, ArXiv:2511.08493.

[6] V. Tripathi, H. Chen, M. Khezri, K.-W. Yip, E. M. Levenson-Falk, and D. A. Lidar, Suppression of crosstalk in superconducting qubits using dynamical decoupling, Phys. Rev. Appl. **18**, 024068 (2022).

[7] J. J. Burnett, A. Bengtsson, M. Scigliuzzo, D. Niepce, M. Kudra, P. Delsing, and J. Bylander, Decoherence benchmarking of superconducting qubits, npj Quantum Inf. **5**, 1 (2019).

[8] J. P. G. van Dijk, E. Kawakami, R. N. Schouten, M. Veldhorst, L. M. K. Vandersypen, M. Babaie, E. Charbon, and F. Sebastiano, Impact of classical control electronics on qubit fidelity, Phys. Rev. Appl. **12**, 044054 (2019).

[9] R. Kueng, D. M. Long, A. C. Doherty, and S. T. Flammia, Comparing experiments to the fault-tolerance threshold, Phys. Rev. Lett. **117**, 170502 (2016).

[10] Á. Márton and J. K. Asbóth, Coherent errors and readout errors in the surface code, Quantum **7**, 1116 (2023).

[11] J. M. Martinis, K. B. Cooper, R. McDermott, M. Steffen, M. Ansmann, K. D. Osborn, K. Cicak, S. Oh, D. P. Pappas, R. W. Simmonds, and C. C. Yu, Decoherence in Josephson qubits from dielectric loss, Phys. Rev. Lett. **95**, 210503 (2005).

[12] A. Agarwal, L. P. Lindoy, D. Lall, F. Jamet, and I. Rungger, Modelling non-Markovian noise in driven superconducting qubits, QST **9**, 035017 (2024).

[13] X. Li, J. Wang, Y.-Y. Jiang, G.-M. Xue, X. Cai, J. Zhou, M. Gong, Z.-F. Liu, S.-Y. Zheng, D.-K. Ma *et al.*, Cosmic-ray-induced correlated errors in superconducting qubit array, Nat. Commun. **16**, 4677 (2025).

[14] D. Ristè, C. C. Bultink, M. J. Tiggelman, R. N. Schouten, K. W. Lehnert, and L. DiCarlo, Millisecond charge-parity fluctuations and induced decoherence in a superconducting transmon qubit, Nat. Commun. **4**, 1913 (2013).

[15] C. Müller, J. Lisenfeld, A. Shnirman, and S. Poletto, Interacting two-level defects as sources of fluctuating high-frequency noise in superconducting circuits, Phys. Rev. B **92**, 035442 (2015).

[16] M. Carroll, S. Rosenblatt, P. Jurcevic, I. Lauer, and A. Kandala, Dynamics of superconducting qubit relaxation times, npj Quantum Inf. **8**, 1 (2022).

[17] F. Berritta, J. Benestad, J. A. Krzywda, O. Krause, M. A. Marciniak, S. Krøjer, C. W. Warren, E. Hogedal, A. Nylander, I. Ahmad *et al.*, Real-time adaptive tracking of fluctuating relaxation rates in superconducting qubits, Phys. Rev. X **16**, 011025 (2026).

[18] T. Thorbeck, A. Eddins, I. Lauer, D. T. McClure, and M. Carroll, Two-level-system dynamics in a superconducting qubit due to background ionizing radiation, PRX Quantum **4**, 020356 (2023).

[19] C. D. Wilen, S. Abdullah, N. A. Kurinsky, C. Stanford, L. Cardani, G. D'Imperio, C. Tomei, L. Faoro, L. B. Ioffe, C. H. Liu *et al.*, Correlated charge noise and relaxation errors in superconducting qubits, Nature **594**, 369 (2021).

[20] R. T. Gordon, C. E. Murray, C. Kurter, M. Sandberg, S. A. Hall, K. Balakrishnan, R. Shelby, B. Wacaser, A. A. Stabile, J. W. Sleight *et al.*, Environmental radiation impact on lifetimes and quasiparticle tunneling rates of fixed-frequency transmon qubits, Appl. Phys. Lett. **120**, 074002 (2022).

[21] S. Schlör, J. Lisenfeld, C. Müller, A. Bilmes, A. Schneider, D. P. Pappas, A. V. Ustinov, and M. Weides, Correlating

decoherence in transmon qubits: Low frequency noise by single fluctuators, Phys. Rev. Lett. **123**, 190502 (2019).

[22] Z. Chen, K. J. Satzinger, J. Atalaya, A. N. Korotkov, A. Dunsworth, D. Sank, C. Quintana, M. McEwen, R. Barends, P. V. Klimov *et al.*, Exponential suppression of bit or phase errors with cyclic error correction, Nature **595**, 383 (2021).

[23] P. V. Klimov, A. Bengtsson, C. Quintana, A. Bourassa, S. Hong, A. Dunsworth, K. J. Satzinger, W. P. Livingston, V. Sivak, M. Y. Niu *et al.*, Optimizing quantum gates towards the scale of logical qubits, Nat. Commun. **15**, 2442 (2024).

[24] B. Shao, X. Yang, R. Liu, Y. Zhai, D. Lu, T. Xin, and J. Li, Multiple classical noise mitigation by multiobjective robust quantum optimal control, Phys. Rev. Appl. **21**, 034042 (2024).

[25] C. L. Edmunds, C. Hempel, R. J. Harris, V. Frey, T. M. Stace, and M. J. Biercuk, Dynamically corrected gates suppressing spatiotemporal error correlations as measured by randomized benchmarking, Phys. Rev. Res. **2**, 013156 (2020).

[26] Andre R. R. Carvalho, H. Ball, M. J. Biercuk, M. R. Hush, and F. Thomsen, Error-robust quantum logic optimization using a cloud quantum computer interface, Phys. Rev. Appl. **15**, 064054 (2021).

[27] Z. Zhang, Z. Miao, and X.-H. Deng, Smolyak-algorithm-assisted robust control of quantum systems with uncertainties, Phys. Rev. A **111**, 042624 (2025).

[28] C.-H. Huang and H.-S. Goan, Robust quantum gates for stochastic time-varying noise, Phys. Rev. A **95**, 062325 (2017).

[29] N. H. Le, M. Cykiert, and E. Ginossar, Scalable and robust quantum computing on qubit arrays with fixed coupling, npj Quantum Inf. **9**, 1 (2023).

[30] H. Xue and X.-H. Deng, Traversing quantum control robustness landscapes: A new paradigm for quantum gate engineering, ArXiv:2412.19473.

[31] M. Harutyunyan, F. Holweck, D. Sugny, and S. Guérin, Digital optimal robust control, Phys. Rev. Lett. **131**, 200801 (2023).

[32] K. Yi, Y.-J. Hai, K. Luo, J. Chu, L. Zhang, Y. Zhou, Y. Song, S. Liu, T. Yan, X.-H. Deng, Y. Chen, and D. Yu, Robust quantum gates against correlated noise in integrated quantum chips, Phys. Rev. Lett. **132**, 250604 (2024).

[33] H. Amer, E. Piliouras, E. Barnes, and S. E. Economou, Implementing and benchmarking dynamically corrected gates on superconducting devices using space curve quantum control, ArXiv:2504.09767.

[34] G. Dridi, K. Liu, and S. Guérin, Optimal robust quantum control by inverse geometric optimization, Phys. Rev. Lett. **125**, 250403 (2020).

[35] H. G. Tonchev, B. T. Torosov, and N. V. Vitanov, Robust, fast, and high-fidelity composite single-qubit gates for superconducting transmon qubits, Phys. Rev. A **112**, 012605 (2025).

[36] H. K. Cummins, G. Llewellyn, and J. A. Jones, Tackling systematic errors in quantum logic gates with composite rotations, Phys. Rev. A **67**, 042308 (2003).

[37] Z.-C. Shi, J.-T. Ding, Y.-H. Chen, J. Song, Y. Xia, X. Yi, and F. Nori, Supervised learning for robust quantum control in composite-pulse systems, Phys. Rev. Appl. **21**, 044012 (2024).

[38] C. Kabytayev, T. J. Green, K. Khodjasteh, M. J. Biercuk, L. Viola, and K. R. Brown, Robustness of composite pulses to time-dependent control noise, Phys. Rev. A **90**, 012316 (2014).

[39] D. Dong, M. A. Mabrok, I. R. Petersen, B. Qi, C. Chen, and H. Rabitz, Sampling-based learning control for quantum systems with uncertainties, IEEE Trans. Control Syst. Technol. **23**, 2155 (2015).

[40] D. Dong, C. Wu, C. Chen, B. Qi, I. R. Petersen, and F. Nori, Learning robust pulses for generating universal quantum gates, Sci. Rep. **6**, 36090 (2016).

[41] M. Cykiert and E. Ginossar, Robust optimal control for a systematic error in the control amplitude of transmon qubits, Phys. Scr. **99**, 105059 (2024).

[42] M. Kuzmanović, I. Björkman, J. J. McCord, S. Dogra, and G. S. Paraoanu, High-fidelity robust qubit control by phase-modulated pulses, Phys. Rev. Res. **6**, 013188 (2024).

[43] E. Berger, V. Maurya, Z. M. McIntyre, K. X. Wei, H. Haas, and D. Puzzuoli, Dimensionality reduction for closed-loop quantum gate calibration, ArXiv:2412.05230.

[44] S. Watanabe, Y. Tabuchi, K. Heya, S. Tamate, and Y. Nakamura, ZZ-interaction-free single-qubit-gate optimization in superconducting qubits, Phys. Rev. A **109**, 012616 (2024).

[45] N. J. Glaser, F. A. Roy, I. Tsitsilin, L. Koch, N. Bruckmoser, J. Schirk, J. H. Romeiro, G. B. P. Huber, F. Wallner, M. Singh *et al.*, Closed-loop optimization for high-fidelity controlled-z gates in superconducting qubits, Phys. Rev. Appl. **24**, 024048 (2025).

[46] M. Werninghaus, D. J. Egger, F. Roy, S. Machnes, F. K. Wilhelm, and S. Filipp, Leakage reduction in fast superconducting qubit gates via optimal control, npj Quantum Inf. **7**, 14 (2021).

[47] C. P. Koch, U. Boscain, T. Calarco, G. Dirr, S. Filipp, S. J. Glaser, R. Kosloff, S. Montangero, T. Schulte-Herbrüggen, D. Sugny, and F. K. Wilhelm, Quantum optimal control in quantum technologies. Strategic report on current status, visions and goals for research in Europe, EPJ Quantum Technol. **9**, 1 (2022).

[48] N. Khaneja, T. Reiss, C. Kehlet, T. Schulte-Herbrüggen, and S. J. Glaser, Optimal control of coupled spin dynamics: Design of NMR pulse sequences by gradient ascent algorithms, J. Magn. Res. **172**, 296 (2005).

[49] S. Machnes, U. Sander, S. J. Glaser, P. de Fouquières, A. Gruslys, S. Schirmer, and T. Schulte-Herbrüggen, Comparing, optimizing, and benchmarking quantum-control algorithms in a unifying programming framework, Phys. Rev. A **84**, 022305 (2011).

[50] F. Motzoi, J. M. Gambetta, P. Rebentrost, and F. K. Wilhelm, Simple pulses for elimination of leakage in weakly nonlinear qubits, Phys. Rev. Lett. **103**, 110501 (2009).

[51] J. M. Gambetta, F. Motzoi, S. T. Merkel, and F. K. Wilhelm, Analytic control methods for high-fidelity unitary operations in a weakly nonlinear oscillator, Phys. Rev. A **83**, 012308 (2011).

[52] F. Motzoi and F. K. Wilhelm, Improving frequency selection of driven pulses using derivative-based transition suppression, Phys. Rev. A **88**, 062318 (2013).

[53] J. Koch, T. M. Yu, J. Gambetta, A. A. Houck, D. I. Schuster, J. Majer, A. Blais, M. H. Devoret, S. M. Girvin, and R. J. Schoelkopf, Charge-insensitive qubit design derived from the Cooper pair box, Phys. Rev. A **76**, 042319 (2007).

[54] E. Hyyppä, A. Vepsäläinen, M. Papič, C. F. Chan, S. Inel, A. Landra, W. Liu, J. Luus, F. Marxer, C. Ockeloen-Korppi *et al.*, Reducing leakage of single-qubit gates for superconducting quantum processors using analytical control pulse envelopes, PRX Quantum **5**, 030353 (2024).

[55] T. E. Skinner and N. I. Gershenzon, Optimal control design of pulse shapes as analytic functions, J. Magn. Res. **204**, 248 (2010).

[56] D. C. McKay, C. J. Wood, S. Sheldon, J. M. Chow, and J. M. Gambetta, Efficient Z gates for quantum computing, Phys. Rev. A **96**, 022330 (2017).

[57] L. Van Damme, A. Devra, E. Malvetti, and S. J. Glaser, GRAPE_SQC, https://github.com/LeoVanDamme/GRAPE_SCQ (2025).

[58] E. Knill, D. Leibfried, R. Reichle, J. Britton, R. B. Blakestad, J. D. Jost, C. Langer, R. Ozeri, S. Seidelin, and D. J. Wineland, Randomized benchmarking of quantum gates, Phys. Rev. A **77**, 012307 (2008).

[59] E. Magesan, J. M. Gambetta, and J. Emerson, Scalable and robust randomized benchmarking of quantum processes, Phys. Rev. Lett. **106**, 180504 (2011).

[60] C. J. Wood and J. M. Gambetta, Quantification and characterization of leakage errors, Phys. Rev. A **97**, 032306 (2018).

[61] J. Kelly, R. Barends, B. Campbell, Y. Chen, Z. Chen, B. Chiaro, A. Dunsworth, A. G. Fowler, I.-C. Hoi, E. Jeffrey *et al.*, Optimal quantum control using randomized benchmarking, Phys. Rev. Lett. **112**, 240504 (2014).

[62] E. Magesan, J. M. Gambetta, B. R. Johnson, C. A. Ryan, J. M. Chow, S. T. Merkel, M. P. da Silva, G. A. Keefe, M. B. Rothwell, T. A. Ohki *et al.*, Efficient measurement of quantum gate error by interleaved randomized benchmarking, Phys. Rev. Lett. **109**, 080505 (2012).

[63] A. M. Stephens, Fault-tolerant thresholds for quantum error correction with the surface code, Phys. Rev. A **89**, 022321 (2014).

[64] S. Sheldon, L. S. Bishop, E. Magesan, S. Filipp, J. M. Chow, and J. M. Gambetta, Characterizing errors on qubit operations via iterative randomized benchmarking, Phys. Rev. A **93**, 012301 (2016).

[65] H. Ball, T. M. Stace, S. T. Flammia, and M. J. Biercuk, Effect of noise correlations on randomized benchmarking, Phys. Rev. A **93**, 022303 (2016).

[66] P. V. Klimov, J. Kelly, Z. Chen, M. Neeley, A. Megrant, B. Burkett, R. Barends, K. Arya, B. Chiaro, Y. Chen *et al.*, Fluctuations of energy-relaxation times in superconducting qubits, Phys. Rev. Lett. **121**, 090502 (2018).

[67] A. P. M. Place, L. V. H. Rodgers, P. Mundada, B. M. Smitham, M. Fitzpatrick, Z. Leng, A. Premkumar, J. Bryon, A. Vrajitoarea, S. Sussman *et al.*, New material platform for superconducting transmon qubits with coherence times exceeding 0.3 ms, Nat. Commun. **12**, 1779 (2021).

[68] C. Wang, X. Li, H. Xu, Z. Li, J. Wang, Z. Yang, Z. Mi, X. Liang, T. Su, C. Yang *et al.*, Towards practical quantum computers: Transmon qubit with a lifetime approaching 0.5 ms, npj Quantum Inf. **8**, 1 (2022).

[69] H. Deng, Z. Song, R. Gao, T. Xia, F. Bao, X. Jiang, H.-S. Ku, Z. Li, X. Ma, J. Qin *et al.*, Titanium nitride film on sapphire substrate with low dielectric loss for superconducting qubits, Phys. Rev. Appl. **19**, 024013 (2023).

[70] M. Bal, A. A. Murthy, S. Zhu, F. Crisa, X. You, Z. Huang, T. Roy, J. Lee, D. v. Zanten, R. Pilipenko *et al.*, Systematic improvements in transmon qubit coherence enabled by niobium surface encapsulation, npj Quantum Inf. **10**, 1 (2024).

[71] S. Ganjam, Y. Wang, Y. Lu, A. Banerjee, C. U. Lei, L. Krayzman, K. Kisslinger, C. Zhou, R. Li, Y. Jia *et al.*, Surpassing millisecond coherence in on chip superconducting quantum memories by optimizing materials and circuit design, Nat. Commun. **15**, 3687 (2024).

[72] M. Mergenthaler, C. Müller, M. Ganzhorn, S. Paredes, P. Müller, G. Salis, V. P. Adiga, M. Brink, M. Sandberg, J. B. Hertzberg, S. Filipp, and A. Fuhrer, Effects of surface treatments on flux tunable transmon qubits, npj Quantum Inf. **7**, 157 (2021a).

[73] M. Mergenthaler, S. Paredes, P. Müller, C. Müller, S. Filipp, M. Sandberg, J. B. Hertzberg, V. P. Adiga, M. Brink, and A. Fuhrer, Ultrahigh vacuum packaging and surface cleaning for quantum devices, Rev. Sci. Instrum. **92**, 025121 (2021b).

[74] O. Dial, D. T. McClure, S. Poletto, G. A. Keefe, M. B. Rothwell, J. M. Gambetta, D. W. Abraham, J. M. Chow, and M. Steffen, Bulk and surface loss in superconducting transmon qubits, Supercond. Sci. Technol. **29**, 044001 (2016).

[75] C. Wang, C. Axline, Y. Y. Gao, T. Brecht, Y. Chu, L. Frunzio, M. H. Devoret, and R. J. Schoelkopf, Surface participation and dielectric loss in superconducting qubits, Appl. Phys. Lett. **107**, 162601 (2015).

[76] J. Lisenfeld, A. Bilmes, A. Megrant, R. Barends, J. Kelly, P. Klimov, G. Weiss, J. M. Martinis, and A. V. Ustinov, Electric field spectroscopy of material defects in transmon qubits, npj Quantum Inf. **5**, 105 (2019).

[77] A. Bilmes, A. Megrant, P. Klimov, G. Weiss, J. M. Martinis, A. V. Ustinov, and J. Lisenfeld, Resolving the positions of defects in superconducting quantum bits, Sci. Rep. **10**, 3090 (2020).

[78] A. Bilmes, S. Volosheniuk, J. D. Brehm, A. V. Ustinov, and J. Lisenfeld, Quantum sensors for microscopic tunneling systems, npj Quantum Inf. **7**, 27 (2021).

[79] Z. T. Wang, P. Zhao, Z. H. Yang, Y. Tian, H. F. Yu, and S. P. Zhao, Escaping detrimental interactions with microwave-dressed transmon qubits, Chin. Phys. Lett. **40**, 070304 (2023).

[80] J. Lisenfeld, A. Bilmes, and A. V. Ustinov, Enhancing the coherence of superconducting quantum bits with electric fields, npj Quantum Inf. **9**, 8 (2023).

[81] P. Zhao, T. Ma, Y. Jin, and H. Yu, Combating fluctuations in relaxation times of fixed-frequency transmon qubits with microwave-dressed states, Phys. Rev. A **105**, 062605 (2022).

[82] Y. Kim, L. C. G. Govia, A. Dane, E. v. d. Berg, D. M. Zajac, B. Mitchell, Y. Liu, K. Balakrishnan, G. Keefe, A. Stabile *et al.*, Error mitigation with stabilized noise in superconducting quantum processors, Nat. Commun. **16**, 8439 (2025).

[83] L. Chen, K.-H. Lee, C.-H. Liu, B. Marinelli, R. K. Naik, Z. Kang, N. Goss, H. Kim, D. I. Santiago, and I. Siddiqi, Scalable and site-specific frequency tuning of two-level system defects in superconducting qubit arrays, ArXiv:2503.04702.

[84] M. Steffen, M. Sandberg, and S. Srinivasan, Recent research trends for high coherence quantum circuits, Supercond. Sci. Technol. **30**, 030301 (2017).

[85] M. Mohseni, A. Scherer, K. G. Johnson, O. Wertheim, M. Otten, N. A. Aadit, Y. Alexeev, K. M. Bresniker, K. Y. Camsari, B. Chapman *et al.*, How to build a quantum supercomputer: Scaling from hundreds to millions of qubits, ArXiv:2411.10406.

[86] S. Gustavsson, O. Zwier, J. Bylander, F. Yan, F. Yoshihara, Y. Nakamura, T. P. Orlando, and W. D. Oliver, Improving quantum gate fidelities by using a qubit to measure microwave pulse distortions, Phys. Rev. Lett. **110**, 040502 (2013).

[87] D. C. McKay, S. Filipp, A. Mezzacapo, E. Magesan, J. M. Chow, and J. M. Gambetta, Universal gate for fixed-frequency qubits via a tunable bus, Phys. Rev. Appl. **6**, 064007 (2016).

[88] M. Roth, M. Ganzhorn, N. Moll, S. Filipp, G. Salis, and S. Schmidt, Analysis of a parametrically driven exchange-type gate and a two-photon excitation gate between superconducting qubits, Phys. Rev. A **96**, 062323 (2017).

[89] P. de Fouquieres, S. Schirmer, S. Glaser, and I. Kuprov, Second order gradient ascent pulse engineering, J. Magn. Res. **212**, 412 (2011).